

We are IntechOpen, the world's leading publisher of Open Access books Built by scientists, for scientists

6,600

Open access books available

178,000

International authors and editors

195M

Downloads

Our authors are among the

154

Countries delivered to

TOP 1%

most cited scientists

12.2%

Contributors from top 500 universities



WEB OF SCIENCE™

Selection of our books indexed in the Book Citation Index
in Web of Science™ Core Collection (BKCI)

Interested in publishing with us?
Contact book.department@intechopen.com

Numbers displayed above are based on latest data collected.
For more information visit www.intechopen.com



Chapter

Heat Transportation by Acicular Micro-Textured Device with Semi-Regular Alignment

Tatsuhiko Aizawa, Hiroki Nakata and Takeshi Nasu

Abstract

Heat transportation device was developed to improve the cooling capacity through the heat convection process and to make low-temperature radiation from the heat source to the objective body in vacuum. This device consisted of the metallic substrate and the acicular micro-/nano-textures in semi-regular alignment. The micro-cone unit cell size and pitch in these textures was controllable by tuning the total current and the current density in the electrochemical processing. Four devices with various unit cell sizes and pitches were prepared for geometric characterization by SEM (Scanning Electron Microscopy) and for spectroscopic analyses on the IR-emittance by FT-IR (Fourier Transform-InfraRed) spectroscopy. Heat radiation experiment was performed to describe the heat transportation in vacuum from the heat source at 323 K to the objective plate. The texture size effect on the low-temperature heat radiation was investigated to build up a physical model for this heat radiation device. Heat convection experiment was also performed to describe the cooling capacity of device under the forced air flow. The unit cell height effect on the cooling behavior was discussed to deduce the physical model for this heat convection device. These models were considered to be used in the computational fluid mechanics simulations.

Keywords: acicular micro-/nano-texturing, heat transportation device, size effect, FT-IR diagnosis, resonance, IR-emission, heat radiation, heat convection, cooling capacity, theoretical model

1. Introduction

Heat transfer and transportation [1–3] is an essential engineering to design the power generator, engines, reactors, and electric devices, to describe the thermodynamic behavior in those systems and units and to develop nontraditional methods for energy saving, reduction of thermal waste, and efficient thermal management. In a sustainable society or in a circular economy toward the zero-carbon wastes and carbon neutrality [4], various mechanical and electrical systems must be designed to significantly minimize the energy consumption and thermal waste, to prevent them from the thermal damages and to prolong their lifetime and make full use of generated heat.

As discussed in [5–8], the graphene solid with higher thermal conductivity than copper was utilized as a thermal spreader from the GaN chips to the substrate in order to preserve the integrity of semiconductor packages. In this heat transportation design, higher thermal conductivity than 1000 W/K was fully utilized for fast and homogeneous thermal spreading to prevent the GaN-chipped package from thermal damages. Let us consider how to improve the heat transfer and transportation capacity in three schemes in **Figure 1**, except for the heat transfer from solid to solid.

The boiling heat transfer in **Figure 1a** advances with the phase transformation from liquid to vapor; its essential behavior is described by the boiling curve. Various approaches [9–11] were proposed to control this relationship between the heat flux (q) and the superheat (ΔT). Among them, the concave and convex micro-textured interface between the copper heater and the cooling water worked to reduce the onset superheat to start the vapor nucleation, to increase the heat penetration rate, and to attain the higher heat flux than the burnout critical limit [12–14].

In the heat convection transfer in **Figure 1b**, the solid interface is cooled down by the natural or forced flow of liquid or gaseous media. Extension of the interfacial area improves the overall heat penetration factor through the interface [15, 16]. In addition, the acicular micro-textured interface is cooled more rapidly than that on the bare copper sheet as stated in [17]. The topological design on the micro-textured interface has large influence on the local convection heat transfer to the coolants.

The heat radiation from the solid to the gaseous media or to the vacuum in **Figure 1c** is driven by emission of electromagnetic waves in the IR (Infrared) wavelength range [18]. In particular, the nano-structured, the meta-material, and the concave micro-textured interfaces [19–21] provided a way to make low-temperature heat radiation. As discussed in [17, 22, 23], the heat radiation takes place at 323 K in air and in vacuum from the acicular micro-textured emitter to the objective body. No temperature rose on the object surfaces when using the bare copper substrate without acicular microtextures. As investigated in [24, 25], the wavelength for IR-emission from the textures with semi-regular alignment of micro-cone shaped unit cells was determined by the resonance condition on the micro-cavity, which was surrounded by micro-cone unit cells under high heat flux. This resonance drives the low temperature heat radiation from the textured surface to objectives with the selected IR-wavelength range.

In the present paper, the micro-cone unit cell size in this acicular micro-texturing is varied to investigate the size effect on the IR-emission. The resonance wavelength range for IR-emission is mainly determined by the micro-cone cell height ($H = H_{ave} + H_{dev}$ for the average height, H_{ave} , and the height standard deviation, H_{dev}). This IR-emission is characterized by the resonance condition via $\lambda \sim 2 \times H$.

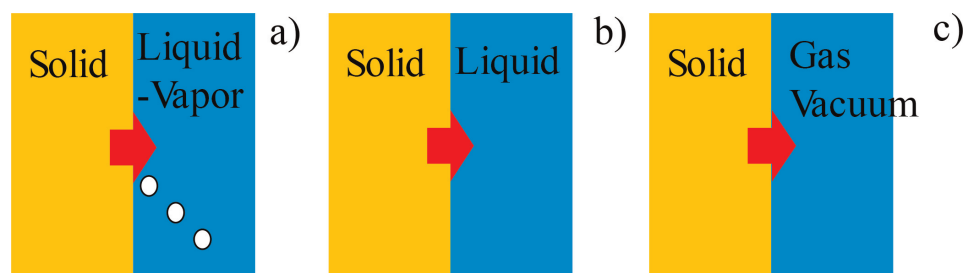


Figure 1. Three heat transfer and transportation schemes from solids to liquid and gaseous media. (a) Boiling heat transfer, (b) heat convection, and (c) heat radiation.

The low temperature heat radiation experiment is performed to describe the heat transportation from IR-emitter to object in vacuum and to discuss the micro-cone cell size effect on the measured thermal transients on the object. The convection heat transfer under forced airflow is also performed to understand the cell size effect on the cooling capacity and the cooling power.

2. Methods and materials

An acicular microtexture is formed onto the copper sheet in semi-regular alignment. Its micro-cone shaped unit cell size is controlled to yield several acicular micro-textured specimens. They are characterized by SEM and FT-IR for geometric measurement and emittance of IR (infrared) electromagnetic waves, respectively. Heat convection and radiation experiments are performed to investigate the unitcell size effect on the cooling capacity and on the low-temperature heat radiation behavior.

2.1 Fabrication of acicular micro-/nano-textured substrate

The electrochemical process was utilized to form the acicular microtextures onto the copper sheet. Iron-nickel ionized solution was used to deposit the Fe-Ni alloy microtextures onto the copper sheet. As schematically depicted in **Figure 2**, the nucleation sites for deposition were first built by the femtosecond laser texturing to control the regularity in the alignment of deposits [26, 27]. Then, the wet plating was performed to make fine micro-texturing. To be discussed later, the micro-cone unit cell size is controlled by the total current and current density in this process.

2.2 Control of micro-cone unit cell sizes

Typical three acicular micro-textured specimens were selected to characterize the micro-cone size and regularity in alignment, using their microstructure observation. **Figure 3** depicts the SEM images for LL-, M-, and SS-specimens, respectively.

Each microtexture is geometrically characterized by the micro-cone cell height (H), the root diameter (B), and the mutual distance (D). The regularity in alignment is also controlled by varying the unit cell size. In the following, {H, B, D} for each acicular microtexture is measured from each SEM image.

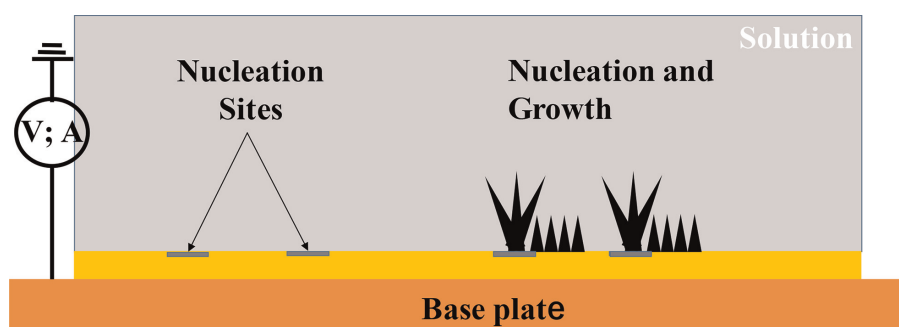


Figure 2.
A schematic view on the electrochemical process with the use of nucleation site control.

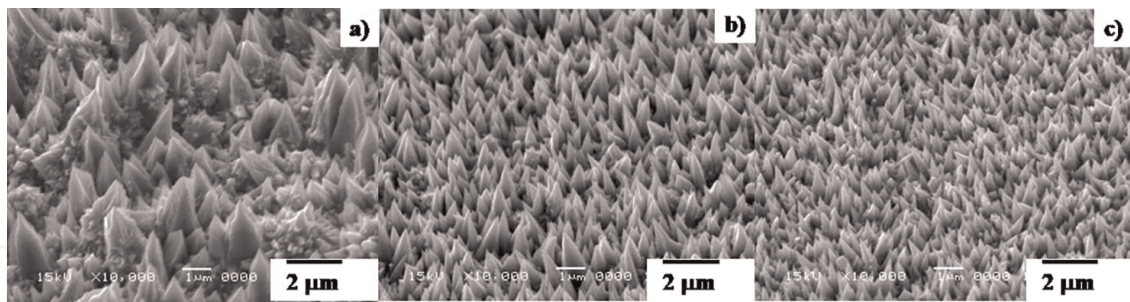


Figure 3. SEM image on the several micro-textured specimens by varying the unit cell sizes [24, 25]. (a) LL-specimen, (b) M-specimen, and (c) SS-specimen.

2.3 Characterization on the acicular microtextures

Using various SEM images with controlling the skew angle, {H, B, D} are estimated with aid of the picture processing [28] and the computational geometry [29]. On the SEM image in plain view, each micro-cone unit cell is identified as a Voronoi polygon by tessellating every micro-cone unit cell. **Figure 4** shows the tessellation process of SEM image to an assembly of Voronoi polygons. The root diameter (B) of each micro-cone cell is determined by the diameter of an inscribing circle to each Voronoi polygon. The mutual distance (D) is calculated by the distancing length between the center points of neighboring Voronoi polygons. On the SEM image with the skew angle of 30°, the whole micro-cone height profile is digitized in pixels. Using the one-to-one correlation between the measured height and the pixels for the same micro-cone unit, the digitized profile is transformed to the height distribution. Hence, {H, B, D} data are determined for each micro-cone unit cell.

The optical properties of acicular microtextures are measured by the FT-IR (Fourier Transform Infra-Red) spectroscopy with reference to the black body. The FT-IR measurement setup is schematically depicted in **Figure 5a**. The detector was placed onto the specimen to measure the transmittance of electromagnetic waves or $T(\lambda)$ in

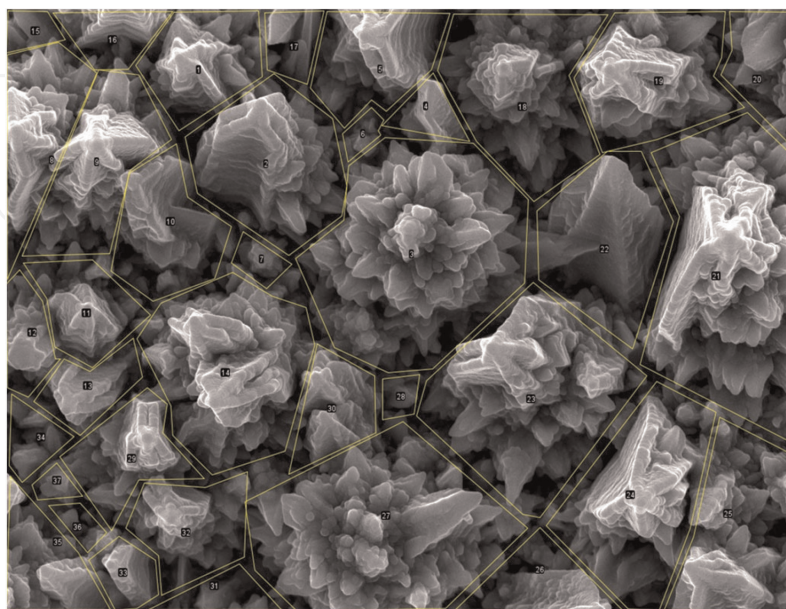


Figure 4. Geometric characterization on the unit cell size and alignment by picture processing and computer geometry [22, 25].

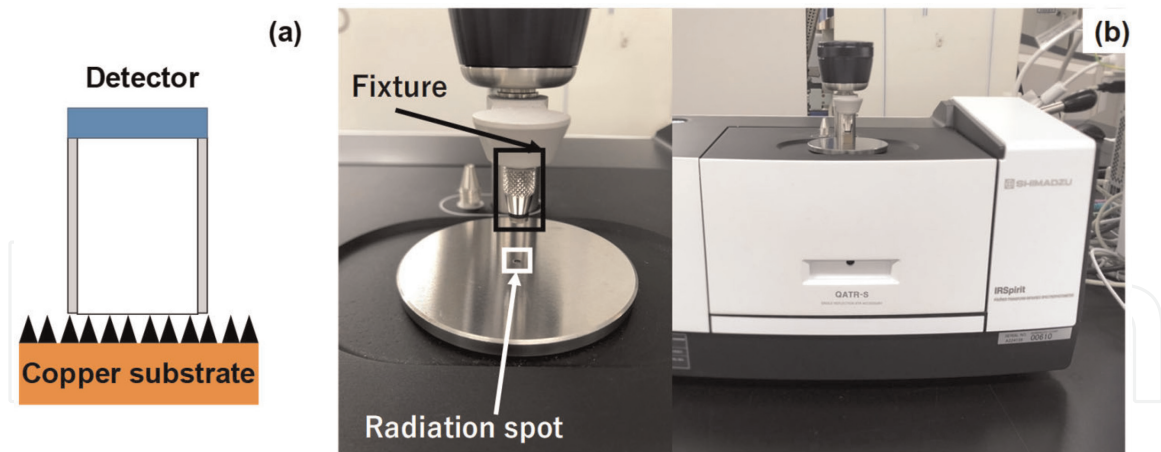


Figure 5. FT-IR spectroscopy to measure the transmittance spectrum of the micro-textured devices. (a) A schematic view of FT-IR spectroscopic analysis, and (b) overview on the FT-IR spectrometer.

the wavelength (λ) range from the visible light to far-IR. As shown in **Figure 5b**, the FT-IR system (IR Spirit; Shimadzu Co., Ltd., Kyoto, Japan) with the detector (QATR-S) was utilized for this spectroscopic measurement. The software (LabSolution IR) was also used to edit the measured raw data and to represent them as a transmittance spectrum, $T(\lambda)$, as the function of the wave number (Λ).

2.4 Heat radiation experiment

The heat radiation process advances from the IR-emitter to an objective body even through the vacuum. In this experiment, the test device was placed onto the hot plate with the holding temperature at 323 K. The black-colored polycarbonate (BC-PC) plate with a thickness of 2 mm was used as an objective body. As depicted in **Figure 6a**, thermography (FLIR-100; FLIR Co., Ltd. Frankfurt, Germany) was

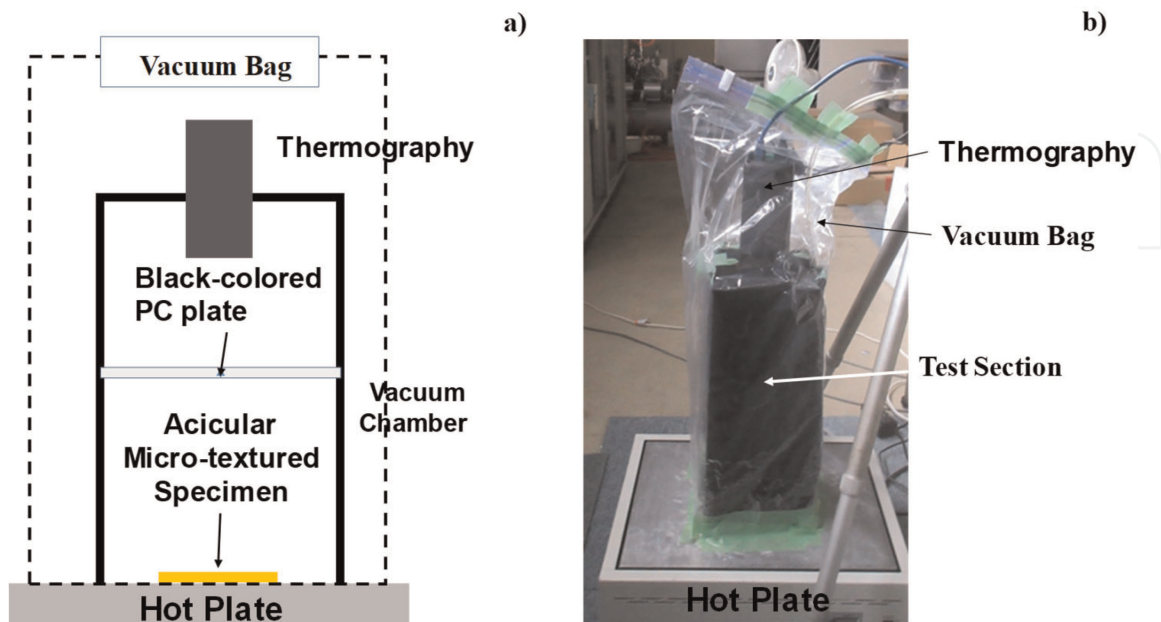


Figure 6. Low-temperature heat radiation experiment in vacuum from the IR-emitter to the objective solid plate. (a) A schematic view of experimental setup, and (b) overview of the experimental setup.

utilized to measure the thermal transients on the top surface of the BC-PC plate. This thermography was focused on the top surface only to measure the thermal transients on it. The whole setup was fully covered by the black cloth to minimize the optical noise. The test-section setup and thermography were all packed into the vacuum bag for evacuation during the experiment. The pressure in the side of bag was kept to be less than 100 Pa. Throughout the experiment, the vacuum bag was continuously evacuated to be free from the heat convection through the residual air.

In experiment, the heat is first transported to the bottom surface of BC-PC plate *via* the heat radiation process. Then, the temperature rises on its top surface by heat conduction from its bottom to its top surface.

When using the bare copper plate instead of a device, no temperature increase was detected on the top surface of the BC-PC plate. This thermal transient measurement was free from a convection heat transfer below the bottom surface of the BC-PC plate. **Figure 6b** shows the overview of the experiment setup for the measurement of the thermal transients on the top surface of the BC-PC plate.

2.5 Heat convection experiment

An experimental setup for heat convection test under the forced air flow was schematically illustrated in **Figure 7a**. **Figure 7b** shows the overview of the whole setup. The specimen was placed on the hot plate with the holding temperature of 50°C or 323 K. The temperature distribution was monitored by thermography. A bare copper plate was utilized as a reference to investigate the cooling behavior under the forced air flow and the temperature recovery process without the air.

3. Results

SEM was utilized to make geometric diagnosis on the acicular microtextures with aid of the picture processing and the computational geometry. IR-emittance was analyzed by FT-IR spectroscopy to discuss the resonance condition between the peak wavelengths in the emittance spectrum and the micro-cone heights. The thermal transportation from the IR-emitter to the object in vacuum was investigated to demonstrate the heat radiation capacity of acicular microtextured device. The convection heat transfer experiment was performed to describe its higher cooling capacity under the forced air.

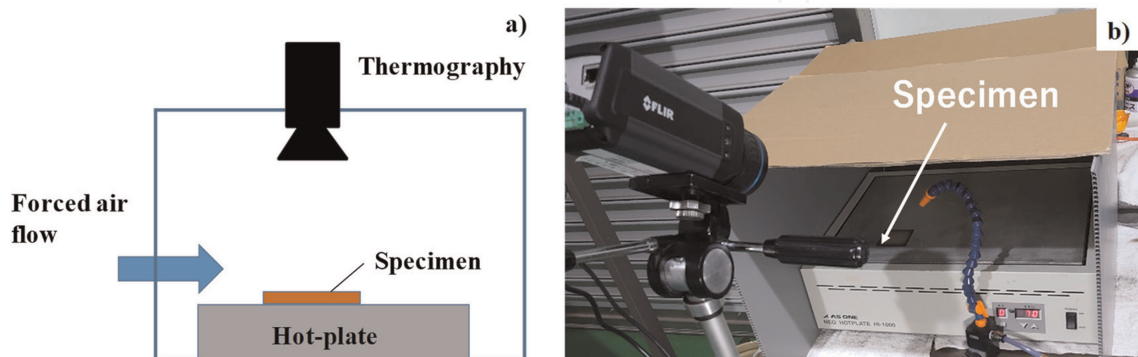


Figure 7. Heat convection experiment under forced air cooling. (a) A schematic view on the experimental setup, and (b) Its overview.

3.1 Geometric diagnosis on the acicular textured device

Four specimens were prepared to have different micro-cone unit cell sizes for geometric diagnosis. At first, the LL-specimen was utilized to make its geometric diagnosis by measurement of the statistical distributions on $\{H, B, D\}$. As shown in **Figure 8a**, the population of micro-cone heights, $P(H)$, has a bimodal distribution with two peaks at $H_{ave} = 2.7 \mu\text{m}$ and $3.5 \mu\text{m}$. The standard deviation is nearly the same between the two profiles; $\Delta H = 0.25 \mu\text{m}$. In **Figure 8b**, $P(B)$ also has a bimodal distribution with two medians at $1 \mu\text{m}$ and $2 \mu\text{m}$. The standard deviation of the first profile is $\Delta B = 0.5 \mu\text{m}$, while it becomes $0.75 \mu\text{m}$ for the second profile. In **Figure 8c**, $P(D)$ has a monotonic distribution with the median at $2.2 \mu\text{m}$ and the standard deviation of $\Delta D = 0.75 \mu\text{m}$. These $P(H)$, $P(B)$, and $P(D)$ as well as $\{H_{ave}, B_{ave}, D_{ave}\}$ and $\{\Delta H, \Delta B, \Delta D\}$ are varied by the regularity control in the alignment of micro-cone unit cells. In the following, $P(H)$, H_{ave} , and ΔH are estimated for other three specimens.

Figure 9 compares the micro-cone unit cell height distributions, $P(H)$, among the M-, S-, and SS-specimens. These $P(H)$ profiles have a mono-modal distribution with the monotonic decrease of H_{ave} to lower heights.

Table 1 summarizes the estimated median, H_{ave} , and standard deviation, ΔH , for these four specimens.

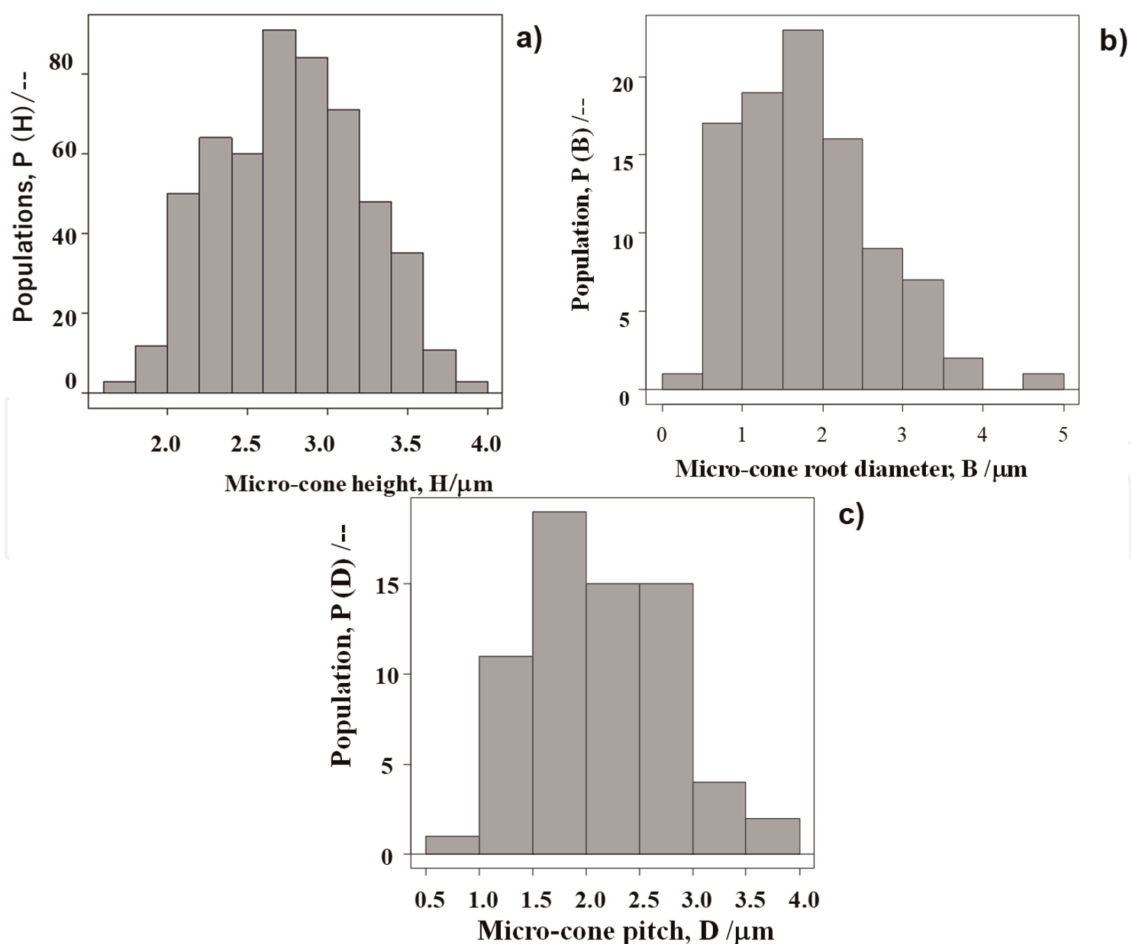


Figure 8. Populations of $\{H, B, D\}$ of micro-cone unit cells in the acicular microtextures for the LL-specimen in Figure 3a [25]. (a) $P(H)$, (b) $P(B)$, and (c) $P(D)$.

| Acicular microtextured specimen | H_{ave} , median in P (H) (μm) | ΔH , standard deviation in P (H) (μm) |
|---------------------------------|---|--|
| LL-specimen | 3.5 | 0.25 |
| LL-specimen | 2.7 | 0.25 |
| M-specimen | 1.3 | 0.2 |
| M-specimen | 0.8 | 0.25 |
| S-specimen | 0.68 | 0.12 |
| SS-specimen | 0.57 | 0.1 |

Table 1. Median and standard deviation of the micro-cone unit cell height distributions for four specimens.

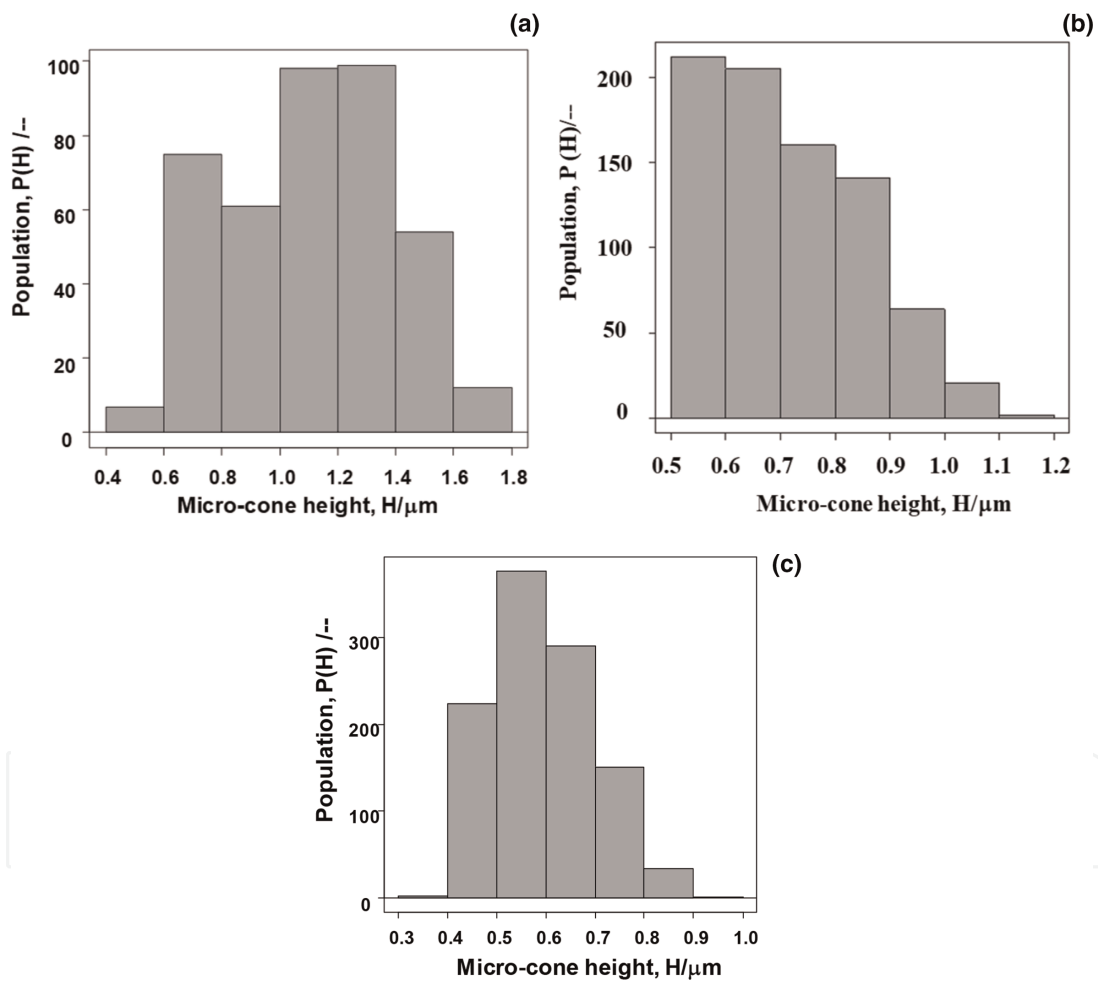


Figure 9. The micro-cone height distribution, $P(H)$, for M-type, S-type, and SS-type acicular microtextured specimens [25]. (a) $P(H)$ for M-type specimen, (b) $P(H)$ for S-type specimen, and (c) $P(H)$ for SS-type specimen.

3.2 Spectroscopic analysis on the IR-emittance from device

The IR-emittance for every acicular micro-textured specimen with the size of 50 mm x 50 mm x 0.5 mm was estimated from the measured IR-transmittance, $T(\lambda)$, by the FT-IR. The measured IR-emittance at the center point of the LL-specimen is shown in **Figure 10**.

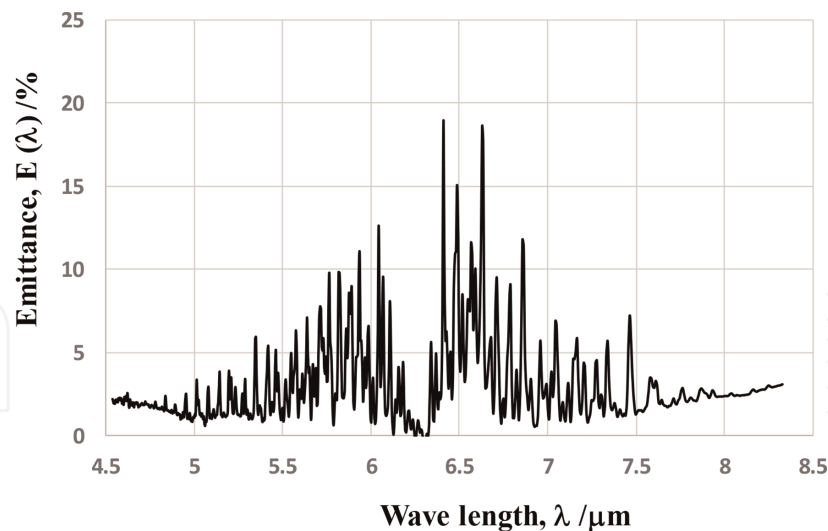


Figure 10.
 The measured IR-emittance by the FT-IR for the LL-type specimen [22, 24, 25].

The IR-emittance $E(\lambda)$ is characterized from the measured transmittance $T(\Lambda)$ by FT-IR in the function of the wavenumber, Λ (cm^{-1}). Since λ (μm) = $10^4/\Lambda$ and $E(\lambda) = 1.0 - T(\lambda)$, $E(\lambda)$ represents the IR-emission from each type of acicular micro-textured specimens. No significant peaks were analyzed for $\lambda < 4.5 \mu\text{m}$ and $\lambda > 8.3 \mu\text{m}$; $T \sim 100\%$ or $E \sim 0\%$ for $\lambda < 4.5 \mu\text{m}$ and $\lambda > 8.3 \mu\text{m}$. In correspondence to the bimodal distribution of $P(H)$ in **Figure 8a**, this $E(\lambda)$ has bimodal profiles, the median of which is located at $\lambda = 5.9 \mu\text{m}$ and $\lambda = 6.7 \mu\text{m}$, respectively. The standard deviation, $\Delta\lambda$, for two profiles is nearly the same as $\Delta\lambda = 0.5 \mu\text{m}$.

As discussed in [22], the measured spectra on the IR-emission at the five positions on the LL-specimen were compared among them. Although the measured intensities deviate from each other, the measure spectra were equivalent to $E(\lambda)$ in **Figure 10**. This implies that the measured $E(\lambda)$ by FT-IR is never dependent on the positions in measurement but intrinsic to the LL-type acicular microtextures in **Figure 3a** with the micro-cone unit cell size distribution in **Figure 8**.

Other three specimens with the same size as the LL-specimen were prepared for FT-IR measurement in the similar manner. The measurement zone was fixed to the center point of every specimen in practice. The wavelength range was only varied to indicate the difference in measured $E(\lambda)$ among three specimens.

In both the LL- and M-type specimens, the IR-emission peaks are detected in their spectra as shown in **Figures 10** and **11a**. The wavelength of this peak shifts to the shorter wavelength, and the peak itself becomes too broad to detect the median of peak directly from the measured spectrum for the S-type specimen in **Figure 11b**. No IR-emission peaks are detected in the measured spectra for the SS-type specimen in **Figure 11c**. As seen in the SEM images on three specimens in **Figure 3**, the shorter micro-cone unit cells align with more regular and dense manner so that less free volume is present among the micro-cone unit cells. **Figure 11** implies that various micro-/nano-texturing parameters of micro-cone unit cells have influence on the IR-emission from the acicular micro-textured film, to be discussed in later.

The average wavelength of emission spectra, λ_{ave} , and the standard deviation $\Delta\lambda$ in each $E(\lambda)$ are estimated from **Figure 11** and listed in **Table 2**.

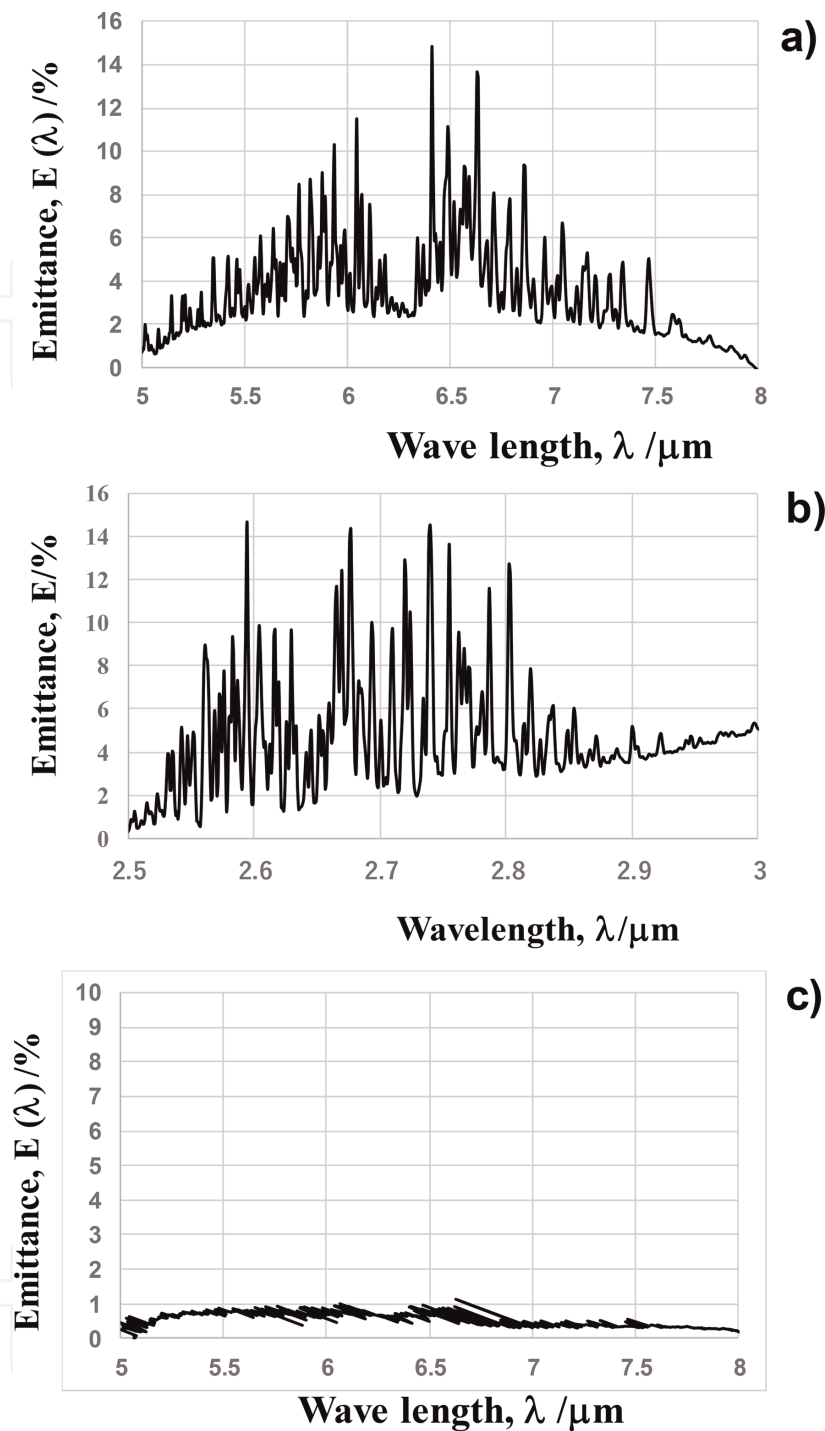


Figure 11. The measured IR-emittance by the FT-IR for M-, S-, and SS-type specimens [25]. (a) $E(\lambda)$ for M-type specimen, (b) $E(\lambda)$ for S-type specimen, and (c) $E(\lambda)$ for SS-type specimen.

Using the data in **Tables 1** and **2**, the correlation between $\{H_{\text{ave}}, \Delta H\}$ and $\{\lambda_{\text{ave}}, \Delta \lambda\}$ is investigated in **Figure 12**.

Within the measured standard deviation $\{\Delta H, \Delta \lambda\}$, the resonance relation for the IR-emission by the acicular microtextured device abides by $\lambda_{\text{ave}} = 2 \times H_{\text{ave}}$ when the emission wavelength is larger than $1 \mu\text{m}$. In the IR-emission with its wavelength shorter than $1 \mu\text{m}$, more precise measurement is necessary to investigate the effect of acicular microtexture size and topology on the IR-emission.

| Acicular microtextured specimen | Average wavelength, λ_{ave} , in IR-emission (μm) | Standard deviation, $\Delta\lambda$, in IR-emission (μm) |
|---------------------------------|--|--|
| LL-type specimen | 6.7 | 0.25 |
| LL-type specimen | 5.9 | 0.25 |
| M-type specimen | 6.5 | 0.4 |
| M-type specimen | 5.7 | 0.4 |
| S-type specimen | 2.7 | 0.7 |
| SS-type specimen | — | — |

Table 2.
 The average wavelength of emission spectra, λ_{ave} and the standard deviation, $\Delta\lambda$ in the measured IR-emission spectra, $E(\lambda)$, for four specimens.

3.3 Thermal transportation via heat radiation

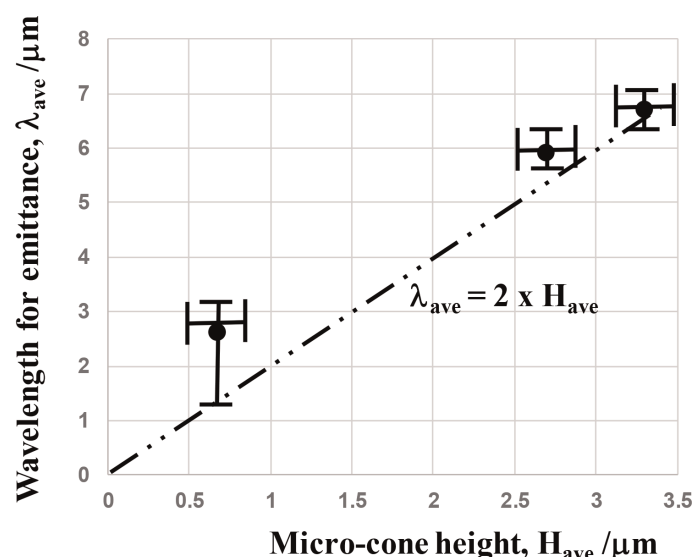


Figure 12.
 Correlation of $\{\lambda_{ave}, \Delta\lambda\}$ in the IR-emission and $\{H_{ave}, \Delta H\}$ in the population of micro-cone unit cell heights to deduce the resonance relation between the resonant IR-waves and the micro-cone unit cells.

The experimental setup in **Figure 6** was first utilized to describe the temperature difference between the heat source and the top surface of acicular micro-textured device. In the following experiment, the former temperature is controlled to be constant by 373 K, while the latter one is determined by the heat flux (q) balance between the q_{inout} from the heat source and q_{output} to the vacuum by the IR-emission. **Figure 13** depicts the stationary temperature distribution, measured by the thermography with its focus onto the LL-specimen surface.

The measured temperature on the acicular micro-textured LL-type specimen decreases down to 323 K, while the heat source surface temperature is constant by 373 K. Due to the IR-emission from the LL-type specimen, the IR-emitter surface temperature is reduced by $\Delta T = 50$ K from the heat source temperature. In the latter, the IR-emission model is discussed with reference to [21, 22, 30]. The physical model for IR-emission from the acicular micro-textured copper plate is also considered for further understanding on the low-temperature heat radiation.

The heat radiation experiment is performed, using the experimental setup in **Figure 6**. Before evacuation, the BC-PC plate with the size of 180 mm x 180 mm x 2

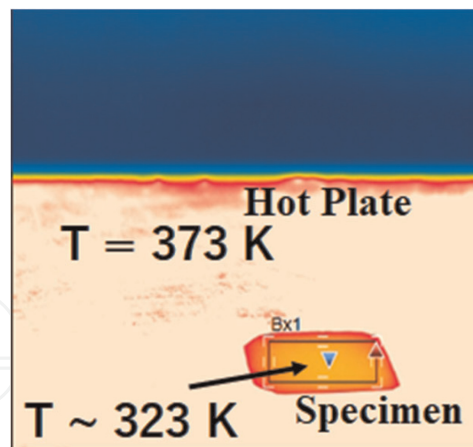


Figure 13. Measurement of the stationary temperature distribution on the heat source (or hot plate) with the micro-textured LL-type specimen. The thermography was focused onto the surface of specimen.

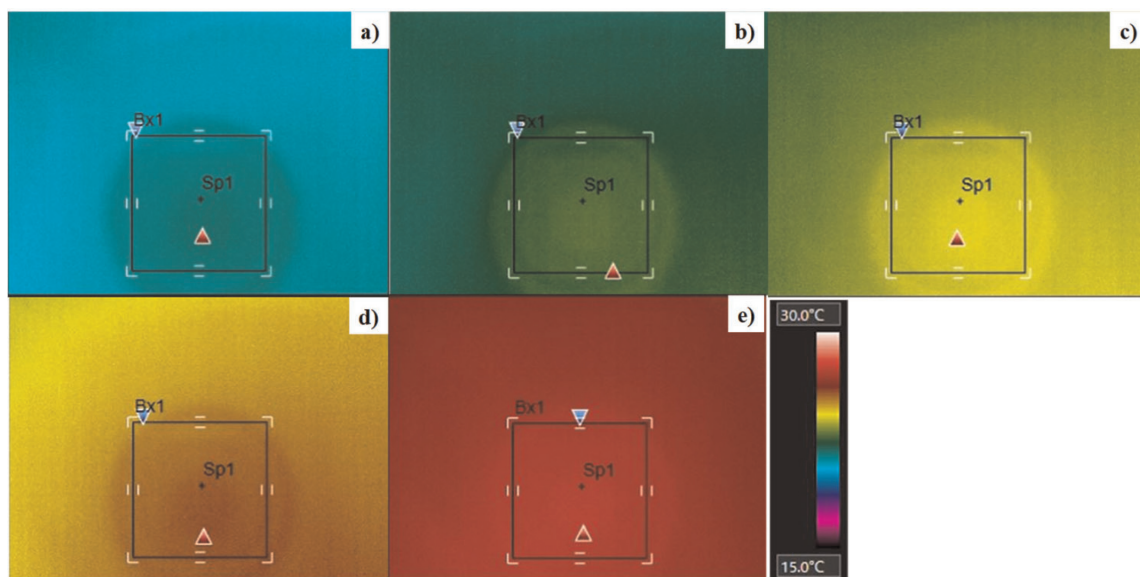


Figure 14. Thermal transient on the top surface of BC-PC plate located away from the LL-type IR-emitter by 150 mm. (a) $\tau = 0$ s, (b) $\tau = 60$ s, (c) $\tau = 120$ s, (d) $\tau = 360$ s, and (e) $\tau = 600$ s.

mmt was placed with the distance from the LL-type micro-textured IR-emitter by 150 mm. The thermography was focused onto the top surface of BC-PC plate.

Figure 14 shows the thermal transient from the onset of measurement at $\tau = 0$ s to the end of measurement at $\tau = 600$ s. In experiment, the measurement starts when the hot plate temperature reaches to 293 K after switching it on; as shown in **Figure 14a**, the surface temperature starts to rise at the center zone of BC-PC plate. During 600 s, the temperature rise reaches 10 K on the top surface of objective body even when the heat source temperature is constant by 323 K as shown in **Figure 14b–e**.

Next, this LL-type specimen is exchanged with the S-type specimen to describe the heat radiation capacity change by reducing the micro-cone heights as shown in **Figures 3** and **12**.

Comparing **Figure 15** for the S-type IR-emitter with **Figure 14** for the LL-type IR-emitter, the thermal transient process is retarded and the final temperature at the hottest spot is reduced by 2 to 3 K. This implies that heat radiation capacity is directly

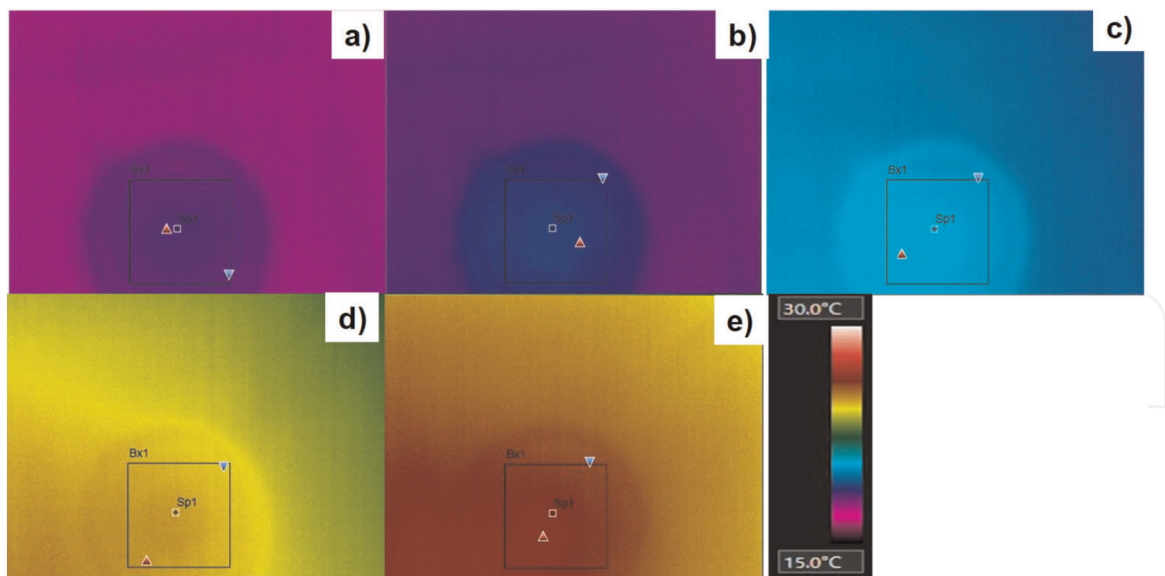


Figure 15. Thermal transient on the top surface of BC-PC plate located away from the S-type IR-emitter by 150 mm. (a) $\tau = 0$ s, (b) $\tau = 60$ s, (c) $\tau = 120$ s, (d) $\tau = 360$ s, and (e) $\tau = 600$ s.

affected by the IR-emission behavior with the micro-cone unit cell size dependency. More heat radiation experiments with higher micro-cone unit cells are necessary to demonstrate the possibility to improve the heat radiation capacity.

3.4 Cooling capacity of convection heat transfer under the forced cooling air

The heat convection under the forced cooling air is performed by using the experimental setup in **Figure 7**. The nozzle was fixed to blow the air in the lateral direction of the micro-textured and bare copper specimens. This air flow was switched on to cool down the specimen surface temperature and switched off to measure the recovery of surface temperature on the specimen. A simple theoretical model is used to describe these cooling and recovery processes of specimen surface temperature.

In this cooling mode, the surface temperature (T) reduces with time from the initial temperature (T_i) down to the lowest temperature (T_L), exponentially. This cooling behavior is modeled by.

$$(T - T_i) / (T_L - T_i) = 1 - \exp(-\kappa_{\text{cooling}} \times \tau), \quad (1)$$

where τ is the transient time from $T = T_i$ to $T = T_L$, and κ_{cooling} represents the cooling capacity of specimen under the forced air-cooling condition. High κ_{cooling} denotes for high cooling rate. This Eq (1) is utilized to estimate this κ_{cooling} by parameter fitting by linear-logarithmically plotting the measured data in experiment. On the other hand, when the forced air blow is stopped, the surface temperature starts to recover from T_L to T_i . This recovery process is also modeled by.

$$(T - T_i) / (T_L - T_i) = \exp(-\kappa_{\text{recovery}} \times \tau), \quad (2)$$

where κ_{recovery} denotes for the recovery constant. In a similar manner to deduce κ_{cooling} , this κ_{recovery} was estimated from the measured data.

Figure 16 summarizes the cooling and recovery responses in the convection heat transfer on the bare copper plate when switching on or off the air blow, respectively. Each experiment was performed three times to deduce the average response with the deviation of measured temperature less than 0.1 K. In a similar manner, four specimens were employed to measure the cooling and recovery responses and to compare the cooling and recovery capacities among four specimens with reference to the bare copper specimen.

Figure 17 depicts the cooling and recovery transients of acicular micro-textured LL-type specimen. Comparing **Figures 16** and **17**, the LL-type textured surface is rapidly cooled down to $T_L < 313$ K (or 40°C) and rapidly recovered to T_i . This reveals that κ_{cooling} and κ_{recovery} of textured copper plate in Eqs. (1) and (2) are more than κ 's of bare copper plate.

Using these cooling and recovery capacities, the heat convection transfer process is compared among four micro-textured copper plates with reference to the bare copper plate. **Figure 18** shows the variation of cooling capacity or κ_{cooling} of four textured specimens with increasing the micro-cone unit cell height. Each κ_{cooling} was measured from the monitored temperature transient data after Eq. (1). When using the SS- and S-specimens, this cooking capacity is enhanced by their dense alignment of shorter micro-cone unit cells. This enhancement is attributed to the enlargement of heat transfer area with reduction of micro-cone size. On the other hand, this capacity also

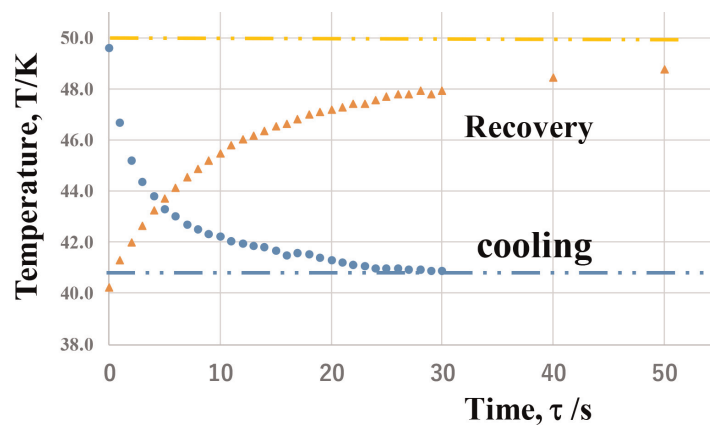


Figure 16. Cooling and recovery responses in the convection heat transfer of bare copper plate when switching on or off the forced air blow, alternatively.

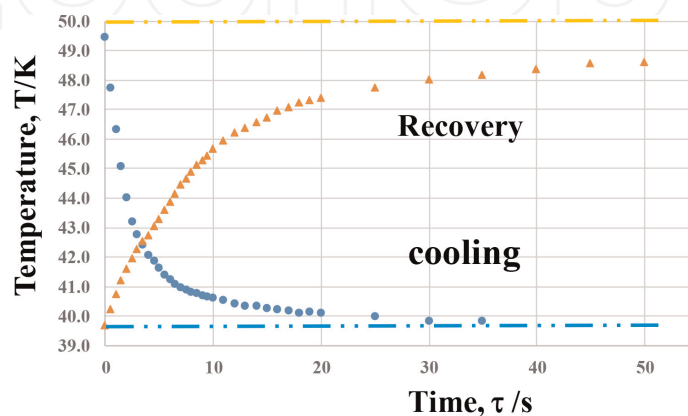


Figure 17. Cooling and recovery responses in the convection heat transfer of the micro-textured LL-type specimen when switching on or off the forced air blow, alternatively.

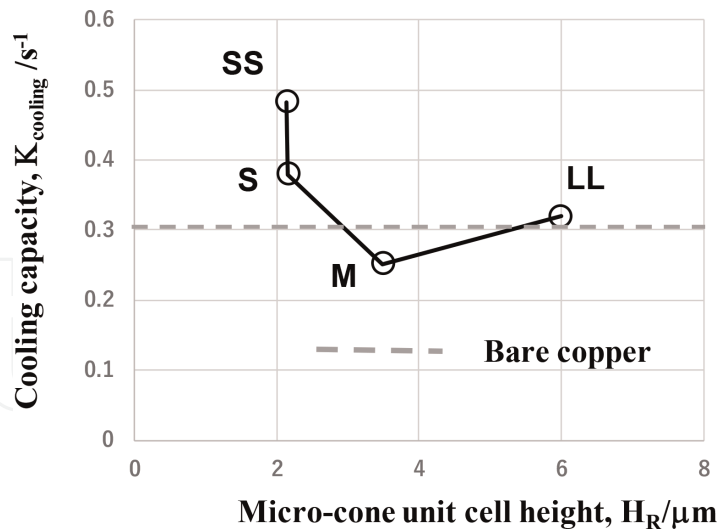


Figure 18.

Comparison of the cooling capacity among four specimens with reference to the bare copper specimen. The representative micro-cone unit cell height, H_R , is equal to H_{ave} for specimens with mono-modal distribution of $P(H)$ and defined by $H_R = (H_{ave}^1 + H_{ave}^2)/2$ for specimens with bimodal distribution of $P(H)$.

increases with increasing the micro-cone unit cell heights. To be remembered, the free volume increases with the micro-texture heights; the micro-cone unit cell density decreases when using the M- and LL-specimens. This implies that the convection heat transfer is enhanced by the forced cooling flow through the microtextures. The convection heat transfer mechanism is expected to change with the acicular microtextures with optimum alignment of micro-cone unit cells and FVEs.

4. Discussion

The acicular micro-textured thin structure with semi-regular alignment of micro-cone unit cells has an IR-emission capability from low-temperature heat source. This IR-emission is driven by the electromagnetic wave resonance with the free volume elements (FVEs) among the acicular microtextures. Since each FVE is surrounded by the micro-cone unit cells, this FVE is wrapped by the metallic walls with high intensity heat flux, as illustrated in **Figure 19a**. Let us estimate this heat flux (q) for IR-emission from the LL-specimen on the heat source. This q is given by $q = -\kappa_a \times (T_S - T_B) / h$, where κ_a is the thermal conductivity of microtextured film, h is the film thickness, and T_S and T_B are the surface and bottom temperatures of micro-textured structure, respectively.

Since the micro-textured structure consists of the Fe-Ni alloy, this κ_a is estimated to be $80 \text{ W} / (\text{m} \cdot \text{K})$. In case of the LL-type specimen, $h = 4 \mu\text{m}$. In the experimental setup in **Figures 6** and **13**, T_B is equal to the hot plate temperature, 373 K , and T_S is the measured temperature, 323 K . Then, each heat flux surrounding the FVE reaches to $1 \text{ GW} / \text{m}^2$ in the physical model in **Figure 19b**. This power dissipates to induce the electromagnetic waves with both nodes at the bottom and top surfaces of free volume elements, respectively. The resonance relationship by $\lambda_R = 2 \times H_R$ in **Figure 12** proves that the electromagnetic waves with the wavelength of λ_R is induced at each FVE among the micro-cone unit cells in the micro-textured film.

In [21, 30], the micro-cavity aluminum sheet was used as an IR-emitter in the heat radiation experiment. The micro-cavity unit cell was sized by $3.5 \mu\text{m} \times 3.5 \mu\text{m} \times 5 \mu\text{m}$.

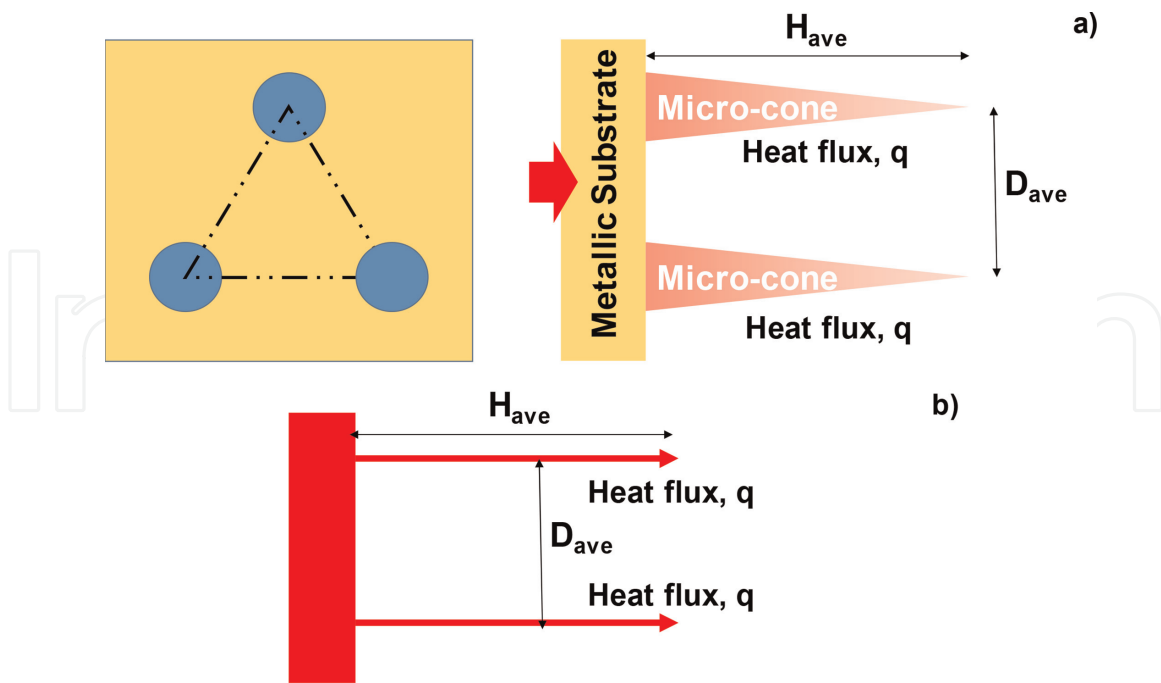


Figure 19. Physical model on the infrared electromagnetic wave resonance in the inside of the free volume, surrounded by the micro-cone unit cells in the micro-textured structure. (a) A schematic view of acicular microtextured IR-emitter, and (b) a physical model of IR-emission.

T_S and T_B were also measured to be $(T_S - T_B) = 10$ K. The IR-emission from this micro-cavity aluminum sheet was detected with reference to the bare aluminum sheet; however, the intensity of IR-emission was still limited in practice. This might be attributed to low resonance of micro-cavity alignment to emit the IR-waves.

Figure 20 illustrates the role of free volume in the IR-emission. When the FVE with the finite volume is present among the micro-cone unit cells, this FVE works as a resonator to emit the IR-waves with the defined wavelength, λ_R , by the resonator height. Notably, the emitted IR-waves simultaneously direct in the vertical direction to the copper substrate in this device. The regularity of micro-textured micro-cone unit cells has much influence on this directivity of IR-waves.

Before further discussion, let us consider the role of free volume element in organic and inorganic materials. As seen in the literature, the free volume element (FVE) works as a key item to determine the functional properties of materials. The free volume fraction plays a key role in the network structure of oxide glasses [31]. In particular, this fraction has a close relationship to the fictitious temperature in the structural relaxation, or to various mechanical and functional properties of oxide glass

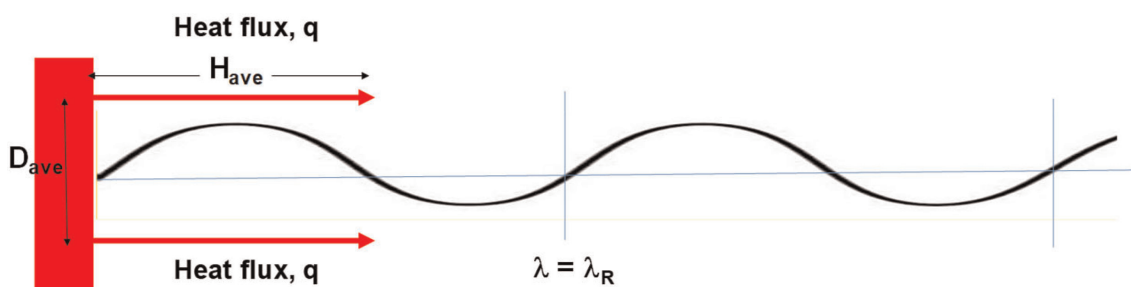


Figure 20. IR-wave emission from each FVE to the vacuum through the resonator voxel. The voxel height defines the emitted IR wavelength.

systems [32]. In the polymer materials such as low-density PMMA (Poly-Methyl--Meta-Acrylate), the nano-scaled FVE induces the ultrafast structural fluctuation in the inside [33]. These findings on the significant role of FVE in various material systems reveal that FVE with a finite volume in the acicular microtextures is responsible for IR-emission through the resonance to drive the electromagnetic waves by the dissipated thermal power to FVE.

Let us consider the micro-cone unit cell size effect on this IR-emission. The resonance relationship in **Figure 12** and the measured IR-emissivity in **Figures 10** and **11** demonstrate that IR-emission is induced for LL-, M-, and S-specimens but that no IR-emission takes place for SS-specimen. SEM images on the microstructures in **Figure 3** show that a free volume is present in the micro-textured film of LL- and M-type specimens but that the micro-cone unit cells align by themselves too densely to induce the electromagnetic waves. This size effect on the IR-emission is physically described by using the FVE model. As illustrated in **Figure 21**, the integrated area ratio, A , of IR-emission spectra per the whole integrated intensity in the all wavelength range decreases with the free volume fraction, f . When using the LL-, M-, and S-specimens, the IR-waves are emitted since f is more than the critical free volume fraction (f_c). However, no IR-emission is detected in **Figure 11c** in the case of the SS-specimen since $f < f_c$.

Various studies were reported in the literature on the microstructural design toward high optical antireflection films [34]. Optical ray simulation was utilized to describe the relationship between the optical reflectivity and the micro-/nano-textured surface. COMSOL software was also utilized to design the anti-reflecting microstructures for IR-applications [35]. The effect of microstructural unit cell shape on the antireflection and its broad band was discussed through the simulation. These studies suggest that the physical model in **Figure 19** is installed into the multi-physics model with consideration to the resonance between the heat dissipation and the IR-emission.

The acicular microtextures control the heat convection mechanism. As stated before, the alignment of micro-cone unit cells or the related size effect to D_{ave} has direct influence on the cooling behavior. With decreasing D_{ave} , the unit cell density increases; the extended surface area enhances the convection heat transfer as depicted in **Figure 22a**. On the other hand, the coolant flow has a structure where the viscous layer at the vicinity of walls has little influence from the main flow. After [13, 14],

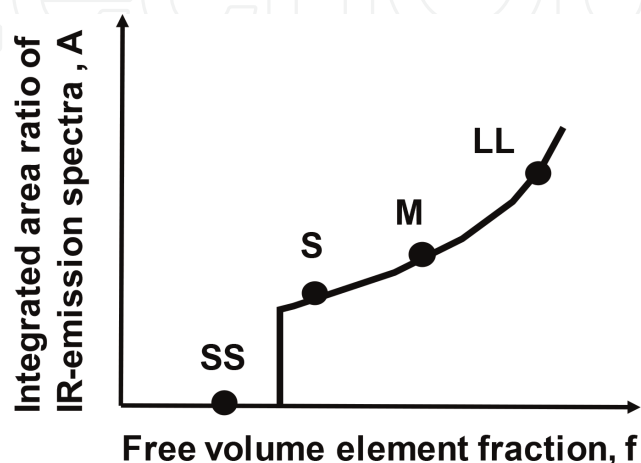


Figure 21.
Free volume element model in the acicular microtextured with different micro-cone unit cell sizes.

when the acicular microtextures are within this viscous layer or the unit cell height is smaller than the viscous layer thickness (y^+), the heat transfer through the microtextures has nothing to do with the main flow of coolant. As depicted in **Figure 22b**, when $H_{ave} > y^+$, the main flow pattern is affected by the acicular microtextures so that the convection heat transfer changes by itself at the presence of microtextures. Three dimensional flow dynamic simulation [36] might be useful to describe this interaction between the coolant flow and the micro-cone unit cells and to theoretically understand the microtexturing effect on the convection heat transfer.

In addition to the microtexture size effect on the convection heat transfer, the topological design is also needed to make full use of acicular microtextures for heat transfer control. In the case of the convex-type acicular microtextures in **Figure 23a**, H_{ave}/B_{ave} and D_{ave}/B_{ave} ratios in $\{H, B, D\}$ -design influence on the heat transfer from the conductively heated micro-cone surfaces to the forced coolant flow. As partially stated in [13, 14], the nucleation site selection of vapors on the micro-cone unit cell surface influences on the bubble density during the boiling heat transfer. This relationship between the acicular microtextures and the vapor nucleation changes by itself by topological change of the convex textures to the concave ones in **Figure 23b**. After the classical boiling heat transfer treatise [9], the vapor was assumed to nucleate itself at the bottom of concave acicular microtextures and to grow in them during the nucleation step in the boiling curve. This suggests the transition of nucleation-to-growth steps of vapors is significantly affected by the concave microtexture sizes.

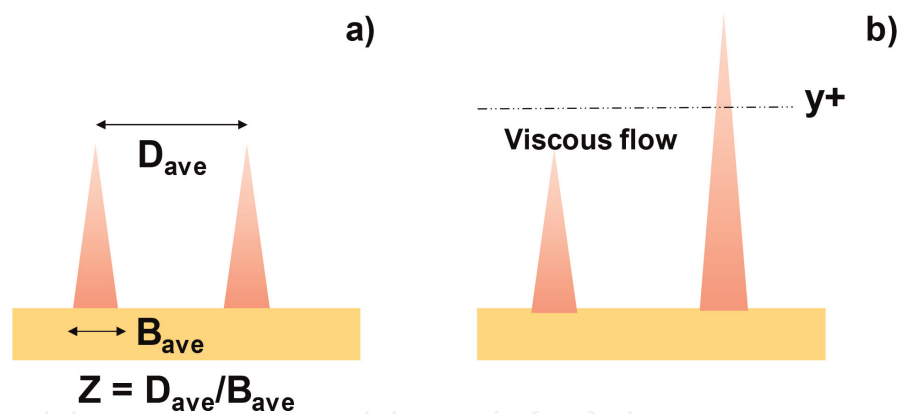


Figure 22. Two types of the microtexturing size effect on the convection heat transfer under the forced coolant flow. (a) Dimensional relationship among $\{H, B, D\}$ in the acicular microtextures, and (b) relationship between the micro-cone height and the viscous flow layer thickness, y^+ .

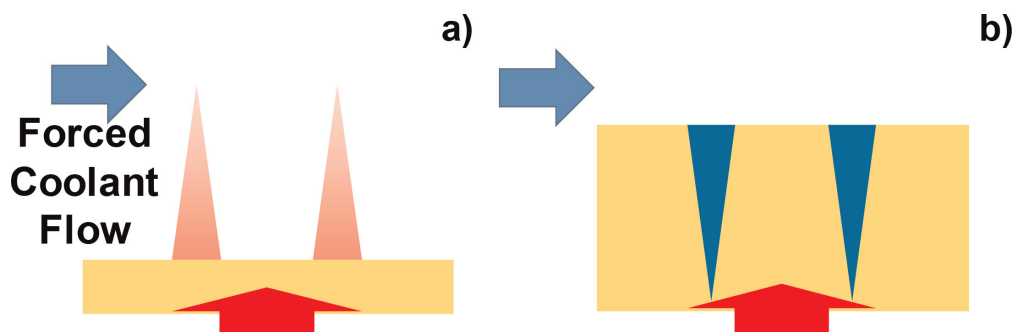


Figure 23. Comparison of the convex and concave acicular microtextures at the convection heat transfer. (a) Convex acicular microtextures, and (b) concave acicular microtextures.

In addition to the acicular microtexture size effect on the IR-emission, let us consider how the micro-cone unit cell regularity influences on this IR-emission. As had been studied in [19, 20], the absorbance or emittance of IR-waves by the nano-structured and meta-material devices was preserved to be nearly 100% in the tailored wavelength range from 1 μm to 5 μm . As shown in **Figure 10**, the maximum emittance is limited by 20 to 30%. This inefficient IR-emission by semi-regularly aligned micro-cone unit cells is attributed to their dispersive distribution with the topological irregularity of FVE. In particular, the geometric and topological distortion of FVEs might significantly reduce the IR-emittance.

The geometric and topological regularity of micro-cones is much improved by the nucleation site control as depicted in **Figure 2**. Their optimum size and shape is investigated to minimize the distortion of FVEs after acicular microtexturing.

Let us summarize the new applications of acicular micro-textured film for thermal transportation and heat transfer.

In the present device, the IR-wave is emitted from each FVE, surrounded by the high heat fluxes. When every micro-cone unit cell is formed onto the curved substrate surface with designated curvature, these emitted IR-waves are focused onto the objective body surface to heat it up by this radiation process, as illustrated in **Figure 24a**. As stated in [35, 37], the acicular micro-textured film with more regular alignment of micro-cone unit cells works as an antireflective device to control the refractive index by its size effect. In **Figure 24b**, the input IR-wave E_1 is transformed to an output IR-wave E_2 by the optical control through the film.

The heat pipe was invented to make long-distance heat transfer from the heat-in section *via* evaporation to the heat-out section *via* condensation [38]. Its inner surface is made of the capillary wick to house the condensate film and the vapor. Preserving nearly the same structure as heat pipe, the vapor chamber is designed as a thin, flat structure unit to make two-phase heat transfer [39]. In its conventional design, the wick is made of the sintered copper layer and copper fins. In both devices, the capillary wick works as an essential structure for evaporation, condensation, and mass flow.

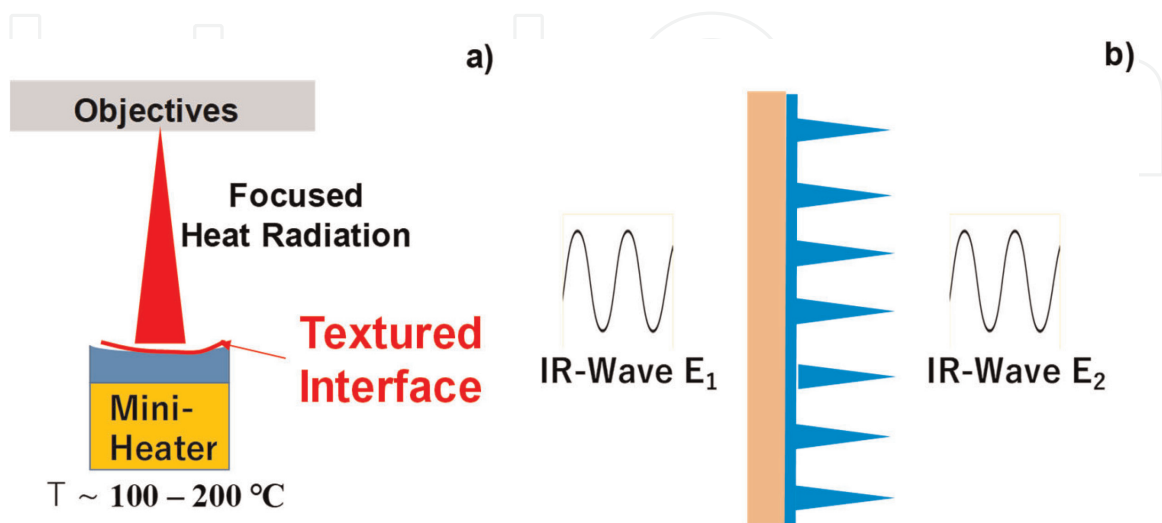


Figure 24. Controllability of radiation heat transfer process and IR-wave transformation. (a) Focusing of emitted IR-waves from the curved microtextured film to the objective body, and (b) antireflection with the tailored refractive index for transformation of IR-waves.

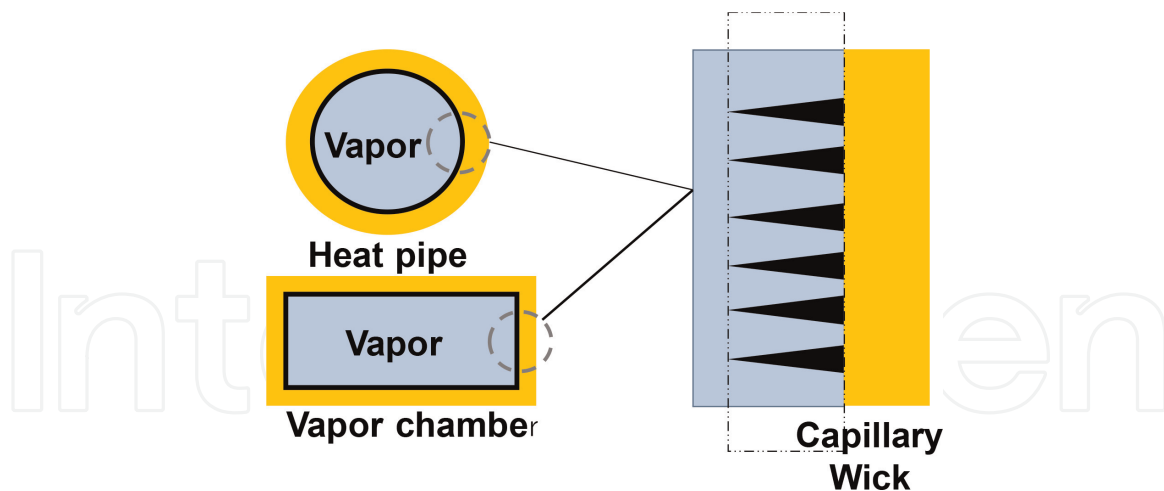


Figure 25.
Controllability of convection heat transfer process in the inside of heat pipe and vapor chamber units.

The inner surfaces of heat pipes and vapor chambers are easily wet-plated by using the present electrochemical procedure, as depicted in **Figure 25**. The micro-cone unit cell sizes are also controllable just in the similar manner as stated before. These Fe-Ni alloy acicular microtextures have sufficient strength and toughness as a structural member. They provide the dense nucleation sites for efficient evaporation and condensation at lower superheat. The flowability of condensate liquids is easily controlled by the micro-cone unit cell sizes.

5. Conclusion

Infrared (IR) optics to terahertz electromagnetics is a new technological field to cultivate the innovative ways onto the basic science and to harvest the valuable applications in heat transfer. The micro-/nano-texturing provides a linkage between this basic understanding on the IR-emission and the heat transportation through radiation. The free volume element (FVE) among the micro-cone unit cells plays a role of IR-emission with the selective wavelength through the resonance of IR-electromagnetic waves to the micro-cone unit cells or the FVE. Since each FVE is surrounded by micro-cone cells with high heat flux, the IR-waves are emitted to have two nodes at the bottom and top of FVE. The wavelength (λ) in this IR-emission is determined to be equal to the doubled FVE-length or the doubled micro-cone heights.

At the presence of resonant free volume element in the acicular micro-textured film, the wavelength of emitted IR electromagnetic waves is controllable from near-IR to far-IR range by varying the micro-cone height. With decreasing the height, the micro-cone unit cells are densely formed on the substrate and the free volume reduces so that IR-emittance significantly decreases and disappears. This size effect of acicular microtextures with semi-regular alignment suggests that more regular alignment is needed to preserve high IR-emittance in the wider selective range of resonant wavelengths.

This acicular microtexturing provides a new way to describe the convection heat transfer process within the viscous layer of coolant or with interaction to the main coolant flow. Various size effects on the single-phase or the two-phase heat transfer between the heating solid and the coolant are experimentally analyzed by using the present device.

In the heat radiation by this acicular micro-textured device, the object located away from the IR-emitter is efficiently heated up till the thermal balance around the objective body. In the heat convection, higher cooling rate is attained by using this acicular micro-textured device. These micotextures are formed on the curved surfaces even with large to be applied to radiation- or convection-based heat transfer of structural members and parts with complex shape and geometry. These are easily mounted and installed as a capillary wick into various heat sinks, heat pipes, and vapor chambers. Phase transformation of cooling media through evaporation and condensation processes is much enhanced together with the control of condensate liquids.

Acknowledgements

The authors would like to express their gratitude to Prof. Ono N. (Shibaura Institute of Technology) and Kurozumi S-I. (Nano-Film Coat, llc.) for their advice and help in experiments.

Conflict of interest

The authors declare no conflict of interest.

Nomenclature

| | |
|-----------------|--|
| A | integrated area ratio of IR-emission spectra in whole spectrum |
| B | root diameter of micro-cone unit cells |
| B_{ave} | median of measured B |
| ΔB | standard deviation of measured B |
| D | mutual distance between adjacent micro-cone unit cells |
| D_{ave} | median of measured D |
| ΔD | standard deviation of D |
| $E(\lambda)$ | emittance in the wavelength, λ |
| H | height of micro-cone unit cell |
| H_{ave} | median of measured H |
| ΔH | standard deviation of H |
| P | population of micro-cone unit cell size parameters {H, D, B} |
| $T(\Lambda)$ | transmittance in the wave number, Λ |
| $T(\lambda)$ | transmittance in the wavelength, λ |
| q | heat flux |
| Λ | wave number in cm^{-1} |
| l | wavelength in μm |
| l_{ave} | median of measured wavelengths |
| $\Delta\lambda$ | standard deviation of measured wavelengths |

IntechOpen

Author details


Tatsuhiko Aizawa^{1*}, Hiroki Nakata² and Takeshi Nasu²

1 Surface Engineering Design Laboratory, Shibaura Institute of Technology, Tokyo, Japan

2 Ebina Denka Kogyo, Co., Ltd., Tokyo, Japan

*Address all correspondence to: taizawa@sic.shibaura-it.ac.jp

IntechOpen

© 2023 The Author(s). Licensee IntechOpen. This chapter is distributed under the terms of the Creative Commons Attribution License (<http://creativecommons.org/licenses/by/3.0>), which permits unrestricted use, distribution, and reproduction in any medium, provided the original work is properly cited. 

References

- [1] Ganji DD, Sabzehmeidani Y, Sedghiamiri A. *Nonlinear Systems in Heat Transfer*. London, UK: Elsevier; 2018
- [2] Frankerwicz M, Golda A, Kos A. Investigation of heat transfer in integrated circuits. *Metrology Measurement System*. 2014;**11**(1): 111-120
- [3] Gong C, Shen J, Yu T, Wang K, Tu Z. A novel radiator structure for enhanced heat transfer used in PEM fuel cell vehicle. *International Journal of Heat and Mass Transfer*. 2020;**157**:119926
- [4] Liang J, Wu J, Guo J, Li H, Zhou X, Liang S, et al. Radiative cooling for passive thermal management towards sustainable carbon neutrality. *National Science Review*. 2022;**10**(1):208
- [5] Saito Y, Aizawa T, Wasa K, Nogami Y. Leak-proof packaging for GaN chip with controlled thermal spreading and transients. In: *Proceedings of the 2018 IEEE BiCMOS and Compound Semiconductor Integrated Circuits and Technology Symposium (BCICTS)*, 15–17 October. San Diego, CA, USA; 2018. pp. 243-246
- [6] Aizawa T, Wasa K, Nogami Y. Plasma oxidation printing into DLC and graphite for surface functionalization. *Journal of Carbon Research*. 2019;**5**(11):1-10
- [7] Aizawa T, Nakata H, Nasu T, Nogami Y. Micro-textured graphitic substrate—copper packaging for robustness. In: *Proceedings of the 5th WCMNM Conference*, September 22, 2022. Leuven, Belgium; 2022. pp. 291-295
- [8] Aizawa T, Nakata J, Nasu T, Nogami Y. Robust packaging of vertically aligned graphite substrate by copper micro-rib structuring. *Journal of Carbon Research*. 2022;**8**(70):1-13
- [9] Kattoh Y. *Fundamentals in Heat Transfer*. Tokyo, Japan: Yokendo; 1964
- [10] Ahn HS, Lee C, Kim H, Jo H, Kang S-H, Kim J, et al. Pool boiling CHF enhancement by micro/nanoscale modification of zircaloy-4 surface. *Nuclear Engineering Design*. 2010;**240**: 3350-3360
- [11] Jung SM, Preston DJ, Jung HY, Deng Z, Wang EN, Kong J. Porous Cu nanowire aerospunges from one-step assembly and their applications in heat dissipation. *Advanced Materials*. 2016; **28**:1413-1419
- [12] Aizawa T, Wasa K, Tamagaki H. A DLC-punch array to fabricate the micro-textured aluminum sheet for boiling heat transfer control. *Journal of Micromachines*. 2018;**9**(147):1-10
- [13] Aizawa T, Ono N. Boiling heat transfer control by micro-/nano-texturing of metallic heat-spreading devices. In: *Proc. 3rd WCMNM2021*, September 21, 2021. Mumbai, India; 2021. pp. 1-10
- [14] Aizawa T, Ono N, Nakata H. Boiling heat transfer on the micro-textured interfaces. *Heat Transfer*. 2022;**2022**: 61-86
- [15] Khalil M, Hassan-Ali MI, Khan KA, Al-Rub RA. Forced convection heat transfer in heat sinks with topologies based on triply periodic minima surfaces. *Case Studies in Thermal Engineering*. 2022;**38**:102313
- [16] Gilmore N, Timchenko V, Menictas C. Manifold microchannel heat

sink topology optimization. *International Journal of Heat and Mass Transfer*. 2021; **170**:121025

[17] Aizawa T, Nakata H, Nasu T. Manufacturing and characterization of acicular Fe-Ni micro-textured heat-transferring sheets. In: Proc. WCMNM2022, September 21, 2022. Leuven, Belgium; 2022. pp. 277-281

[18] Bergman TL. Active daytime radiative cooling using spectrally selective surfaces for air conditioning and refrigeration. *Solar Energy*. 2018; **174**:16-23

[19] Li W, Fan S. Nano-photonic control of thermal radiation for energy applications. *Optics Express*. 2018; **26**: 15995-16021

[20] Tian Y, Ghanekar A, Ricci M, Hyde M, Gregory O, Zheng Y. A review of tunable wavelength selectivity of metamaterials in near-field and far-field radiative thermal transport. *Materials*. 2018; **11**:862

[21] Kohiyama A, Shimizu M, Yugami H. Unidirectional radiative heat transfer with a spectrally selective planar absorber/emitter for high-efficiency solar thermos-photovoltaic systems. *Applied Physics Express*. 2016; **9**: 112302

[22] Aizawa T, Nakata H, Nasu T. Fabrication and characterization of acicular micro-textured copper sheet device for low-temperature heat radiation. *Journal of Micromachines*. 2023; **14**(507):1-12

[23] Aizawa T, Nakata H, Nasu T. Acicular microtexturing onto copper sheet for heat radiation. In: Proc. 12th AWMFT Conference, May 17, 2023. Gangneung, Korea; 2023. p. 67

[24] Aizawa T, Nakata H, Nasu T, Mitohka Y. Acicular microtextured sheet device for heat radiation with controlled unit-cell size and regularity. In: Proceedings of the 5th WCMNM Conference, September 20, 2023. Evanston, USA; 2023. pp. 5-99 (in press)

[25] Aizawa T, Nakata H, Nasu T. Infra-red emission from micro-cone textured metallic sheet with semi-regular alignment. *Journal of Photonics*. 2023 (in press)

[26] Aizawa T, Inohara T. Pico- and femtosecond laser micromachining for surface texturing. In: *Micromachining*. London, UK, London, UK: IntechOpen; 2019. pp. 1-24

[27] Aizawa T, Inohara T, Wasa K. Fabrication of superhydrophobic stainless steel nozzles by femtosecond laser micro-/nano-texturing. *International Journal of Automation Technology*. 2020; **14**(2):159-166

[28] Oho E. Digital image processing technology for scanning electron microscopy. *Advances in Imaging and Electron Physics*. 1998; **105**(77-112): 113-140

[29] Preparata FP, Shamos MI. *Computational Geometry*. New York, USA: Springer; 1985

[30] Okitsumo Co., Ltd. Development of Net Heatsink Type Thermal Emission Materials. Japan: METI; 2013. pp. 1-54

[31] Suzuki S, Takahashi M, Hikich Y. Free volume of network-forming oxide systems $P_2O_5 - (GeO_2, TeO_2, Sb_2O_3, V_2O_5)$. *Journal of the American Ceramic Society*. 1987; **70**(9):C213

[32] Nishida T, Kubuki S, Oka N. Local structure, glass transition, structural relaxation, and crystallization of

functional oxide gasses investigated by Moessbauer spectroscopy and DTA. *Journal of Material Science*. 2021;**32**: 23655-23689

[33] Hoffman DJ, Fica-Contreras SM, Fayer MD. Amorphous polymer dynamic and free volume element size distributions from ultrafast IR spectroscopy. *PNAS*. 2020;**117**(25): 13949-13958

[34] Chen T, Wang W, Pan A, Hu L, Mei X. Characterization of anti-reflection structures fabricated via laser micro/nano-processing. *Optical Materials*. 2022;**131**:112686

[35] Pal U. Designing antireflecting microstructures for infrared applications. COMSOL Blog. Available from: <https://www.comsol.com/blogs/designing-antireflecting-microstructures-for-infrared-applications/> [Accessed May 23, 2023].

[36] Yamada T, Ono N. A study on micromixing utilizing Marangoni effect induced on gas-liquid free interfaces. *Journal of Micro-/Nano-manufacturing*. 2015;**3**:021003

[37] Lopez-Alonso JM, Mandviawala T, Alda J, Lail B, Boreman G. Infrared antenna metrology. *Proceedings of SPIE*. 2005;**5987**:59870L1-59870L11

[38] Bahman Z. Basic principles of heat pipes and history. In: *Heat Pipe Design and Technology*. Springer; 2016. pp. 1-41

[39] Peterson GP, Ma H. Chapter one – Advances in vapor chambers and phase change heat spreaders. *Advances in Heat Transfer*. 2021;**53**:1-96